PAPER

Plasmonic enhancement of photocurrent generation in two-dimensional heterostructure of WSe$_2$/MoS$_2$

To cite this article: Soheil Ghods and Ali Esfandiar 2021 *Nanotechnology* **32** 325203

View the article online for updates and enhancements.

You may also like

Plasmonic enhancement of photocurrent generation in two-dimensional heterostructure of WSe$_2$/MoS$_2$

Soheil Ghods and Ali Esfandiar

Department of Physics, Sharif University of Technology, Tehran 11155-9161, Iran

E-mail: esfandiar@physics.sharif.edu

Abstract

Enhancing the photoresponse of single-layered semiconductor materials is a challenge for high-performance photodetectors due to atomically thickness and limited quantum efficiency of these devices. Band engineering in heterostructure of transition metal chalcogenides (TMDs) can sort out part of this challenge. Here, we address this issue by utilizing the plasmonics phenomenon to enrich the optoelectronics property of the WSe$_2$/MoS$_2$ heterojunction and further enhancement of photoresponse. The introduced approach presents a contamination-free, tunable and efficient way to improve light interactions with heterojunction devices. The results showed a 3600-fold enhancement in photoresponsivity and a 46-fold increase in external quantum efficiency (549%) along with a fast photoresponse time ($\sim$2 μs) and light polarization dependence. This improvement may assign to multiple light scatterings by the Au nanoarrays and creation of strong local electrical fields (hot spots) at the interfaces of the gold nanoarrays and the TMDs heterostructure. The high-energy electrons (hot electrons) originating from hot spots surmount easily to conduction bands of heterojunction which is leading to a remarkable enhancement of photocurrent. The plasmons assisted photoresponse strategy can be easily matched with the semiconductor industry to boost the performance of optoelectronics devices for practical applications.

Supplementary material for this article is available online

Keywords: heterostructure, hot electrons, photoresponse, dimer plasmonic nanoarrays, light polarization

(Some figures may appear in colour only in the online journal)

1. Introduction

After isolation of graphene as zero energy bandgap two-dimensional material from graphite in 2004 [1], transition metal dichalcogenides (TMDs) attract vast attention as layered semiconducting nanostructures with tunable electronic and optical properties [2] in which their energy bandgaps can be tuned by the number of layers, electrostatic and chemical doping [3, 4]. Among large members of the TMDs family such as MoS$_2$, MoSe$_2$, WS$_2$ and WSe$_2$ are emerging as exciting systems for a new generation of ultrathin optoelectronics and photovoltaic devices in visible wavelength range such as photodetectors [5], lasers [6], solar cells [7], light-emitting diode [8], electroluminescence emission [9] and polarizers [10]. In this regard, the monolayers of the TMDs are particularly more interesting for photon detection due to their direct and larger energy band gaps [11]. In the application point of view, the photodetectors play important roles in many fields of our daily life including electro-optical displays, imaging, environment monitoring, optical communication, military, etc [5]. Despite all these promising points, photodetectors fabricated by monolayers of TMDs are suffering from some drawback points such as low light absorption (0.2% in the best situation) [12] lack of intrinsic charge carriers ($\sim$10^{12} cm^{-2}) [13], small wavelength detectivity [5] and low speed of photoresponse [14].

The heterostructures of the TMDs as a novel approach and artificial assembly of two-dimensional materials can compensate some of these issues. In well-matched energy band alignment of heterojunction, increased light absorption [15], more charge carriers separation (less recombination of photo-generated carriers) [16, 17], and wavelength range selectivity [5, 18]. These advantages have made these structures as potent candidates for fundamental and applied researches and the new class of photodetectors and photo-transistors [5, 19]. One of the most amazing heterostructures among TMDs is the WSe$_2$/MoS$_2$ heterostructure due to its exceptional energy band alignment, relatively high carrier mobility (~200 cm^{2}V^{-1}s^{-1}) [20], high light absorbance (~10%) [15] and well-defined current rectification effects (rectification ratio ~10^4) [21]. Due to these features, photo-detectors based on WSe$_2$/MoS$_2$ heterostructure displays the photoresponsivity of 0.05 A W^{-1}, external quantum efficiency (EQE) of 12% in the wavelength range of 514 nm-633 nm [22].

However, further improvement of the photoresponsivity and EQE in WSe$_2$/MoS$_2$ heterostructure has been hindered by the limited low light adsorption coefficient, insufficient scattering and reflection of the incident light at the interface. Since plasmonic nanostructures are well-known as potent light harvesters, this challenge can be surpassed by plasmonic properties of the Nobel metallic nanoparticles by modifying their size and shapes. Here, we have utilized gold (Au) nanodots as plasmonic arrays to intensify light interactions in the WSe$_2$/MoS$_2$ heterostructure. Using Au nanoarrays as an optically active substrate, we could boost the photo-responsivity and reduce the response times. This approach can push further the TMDs based heterostructures towards real application in photon detections.

2. Experimental methods

The Au nanoarrays on SiO$_2$ (~300 nm)/Si substrate were prepared by electron beam lithography process on spin-coated Poly (methyl methacrylate) (C3 PMMA 950K Microchem corp.) following by physical vapor evaporation of Cr (2 nm)/ Au (30 nm). The periodic Au nanoarrays as pairs of gold nanoparticles denoted as dimer arrays of Au nano-dots in a rectangular lattice can be obtained by liftoff step in acetone. Then, mechanically exfoliated flakes (WSe$_2$ and MoS$_2$) from their high-quality crystals (hq graphene) on PMMA/PVA film, were transferred on Au nanoarrays using a home-made transferring system. Finally, the electrodes were deposited on both sides of the heterostructure through standard photo-lithography and Cr/Au deposition by electron gun evaporator.

Electrical characterization of the devices was recorded by KEITHLEY 6487 picoammeter voltage source instrument. To evaluate time response of the device, a pulsed light has been used controlled by GWINSTEK GDS-1052-U oscilloscope along with a current to voltage converter circuit. In the UV-to-NIR region, 13 LEDs were employed to illuminate the

samples by wavelengths of 395, 415, 435, 445, 470, 510, 520, 595, 625, 650, 735, 850, and 970 nm.

3. Results and discussion

Figure 1 demonstrates the design and images of the device fabrication steps. It schematically shows the structure of a hybrid photodetector based on heterostructure of WSe$_2$/MoS$_2$ and Au nanoarrays. Figure 1(b) also depicts the cross-section of this device. On top of Au nanoarrays, the WSe$_2$/MoS$_2$ heterojunction is transferred and the Ti/Au contacts are taken from two layers of WSe$_2$ and MoS$_2$. The field emission scanning electron microscopy (FE-SEM; TeScan–Mira III) image of Au nanoarrays has been illu-strated in figure 1(c). As shown in figure 1(d), the Au nanoarrays consist of dimer (pairs) arrays of circular dots which are arranged on the Si/SiO$_2$ substrate. The inter-distance between the Au nanoparticles (edge-to-edge separation) in each dimer array was ~25 nm (as shown in the inset of figure 1(d)), and the lattice spacing of the Au arrays in the horizontal and vertical directions were 300 and 500 nm, respectively. Figure 1(e) demonstrates the optical microscopy image of the device. The MoS$_2$ flake (red dashed line in a figure 1(e)), and WSe$_2$ flake (green dashed line in a figure 1(e)) are labeled to highlight the device structure. A top view optical image of the device with electrical contacts is depicted in figure 1(f). One of the contacts was taken from the upper flake (WSe$_2$) and another contact was from another flake (MoS$_2$).

To do topography analysis of the flakes on Au nanoar-rays, atomic force microscopy (AFM, Park Scientific CP-Research, VEECO) was used (as shown in figure 2(a)). Figure 2(b) represents step-height profiles of the WSe$_2$ flakes on Au nanoarrays. The red line shows height profile of the deformed flakes on a physical gap of the Au dimer islands and the blue line indicates the area containing no flake. According to the height profile in figure 2(b), the thickness of the Au dots is ~30 nm, and the difference of 20 nm between the two profiles originating from flake sagging. These deformations of the flakes around Au nanoarrays produce tensile strain (~ < 2%) which reduce the band gap of the flakes (~ 0.2 eV) [23, 24] (see S1 section (available online at stacks.iop.org/ NANO/32/325203/mmedia)). The SEM image of trans-ferred flakes on Au nanoarrays proves the presence of the flakes on Au nanoarrays as a black area. Raman analysis is a potent technique to investigate the fingerprint vibrational modes of 2D materials. To Raman spectra acquisition from the heterostructure area, a confocal Raman scattering micro-scopy (Witech Alpha300 R) was utilized by a laser wave-length of 532 nm as an excitation source at room temperature (figure 2(d)). The Raman spectrum indicates characteristics peaks at 380 cm^{-1} and 408 cm^{-1} corresponding to MoS$_2$ monolayer flake assigning to E$_{2g}^1$ and A$_{1g}$ modes, respec-tively. Moreover, the peaks centered at 250 cm^{-1} and 260 cm^{-1} attributes to the monolayer of the WSe$_2$, corresp-onding to the E$_{2g}^1$ and A$_{1g}$ modes of the WSe$_2$ mono-layer [25].
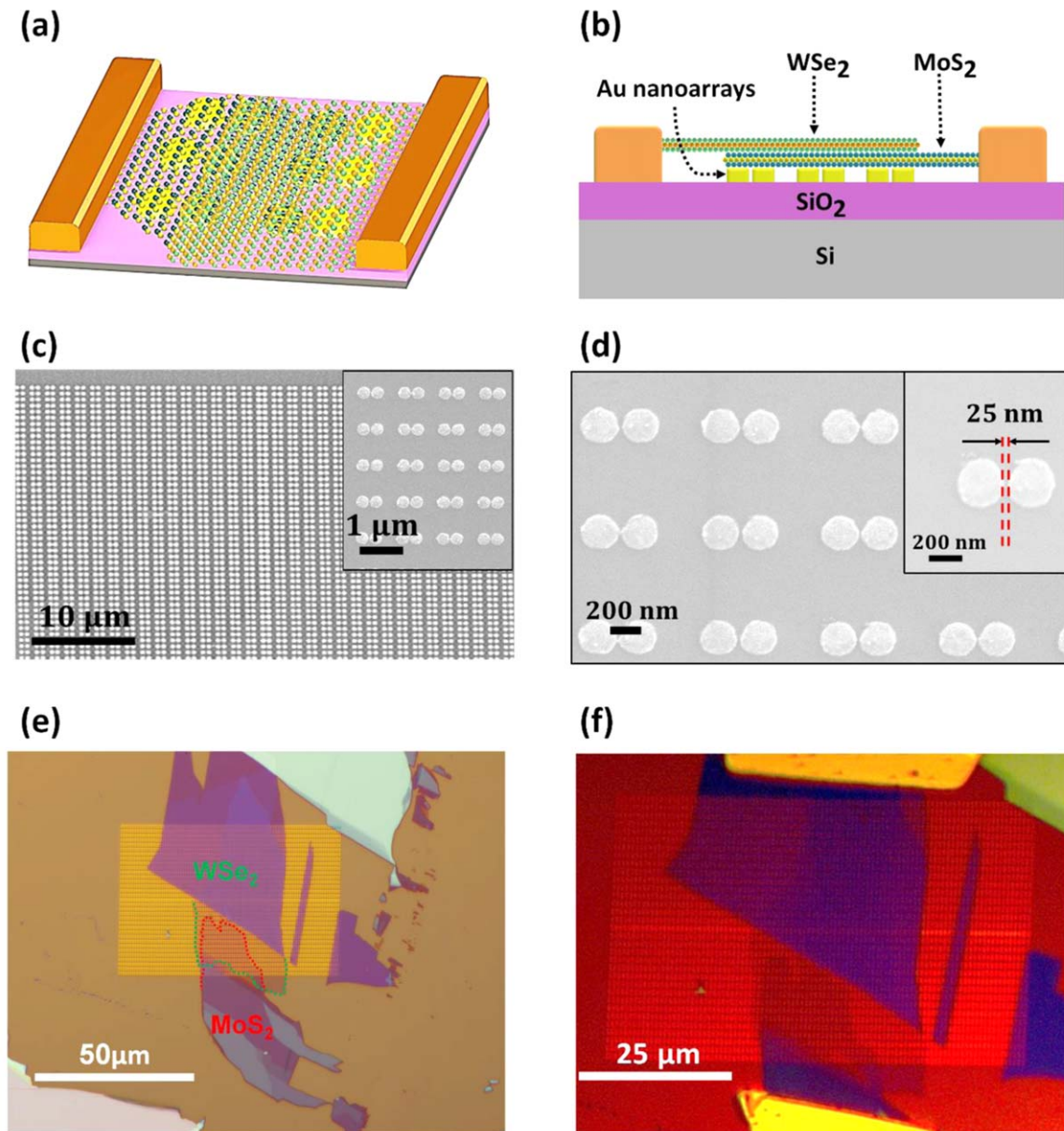
Figure 1. (a) A schematic illustration of WSe$_2$/MoS$_2$ vertical heterojunction and Au nanoarrays. (b) The schematic demonstrates cross-section of the WSe$_2$/MoS$_2$ heterojunction and Au nanoarrays. (c) SEM image of Au nanoarrays. (d) SEM image with higher magnification from Au nanoarrays. (inset shows the dimer structure of Au nanoparticle) (e) Optical image of WSe$_2$/MoS$_2$ /Au nanoarrays device, with WSe$_2$ layer specified by the green line and MoS$_2$ layer by a red line. (f) optical image of the final device after electrodes fabrication.

The $I-V$ characteristics of the heterostructure device are shown in figure 3 as logarithm and linear scales. In general, the energy barrier (0.38 eV) created for the holes is less than electrons (0.55 eV) due to the difference in the bandgap and band alignment between conduction and valence bands of the MoS$_2$ and WSe$_2$ flakes [26]. In reversed regime marked as A in figure 3(a), the electrons tend to transfer from the WSe$_2$ valence band to the conduction band of the MoS$_2$. This mechanism is so-called band-to-band tunneling (BTBT) [27], which leads to tunneling of charge carriers through the barrier to have a contribution in electrical conduction. In regime B as an unbiased state, the charge carriers are hindered by the potential barrier and cause much smaller current values. At low forward bias (regime C), the holes in the WSe$_2$ can

transport to the MoS$_2$ valence band and leading to an increase in the electrical conduction. However, few electrons overcome the potential barrier and participate in the conduction. As the forward bias increases, the MoS$_2$ conduction band shifts upwards, so that more electrons and holes can participate in the conduction (Region D in figure 3(a)) [25, 28]. In the C and D sections of figure 3, direct tunneling takes place. To explain this kind of tunneling, the current-voltage diagram is drawn as a double-log curve. (inset of figure 3(b)) Two linear regimes can be observed in the forward bias region: 0.02 V < V_{ds} < 0.1 V with a slope of ~0.27 and 0.3 V < V_{ds} < 1.5 V with a slope of ~0.52. This gives us an estimation of the depletion layer thickness in the WSe$_2$/MoS$_2$/Au nanoarrays structure. Under low and
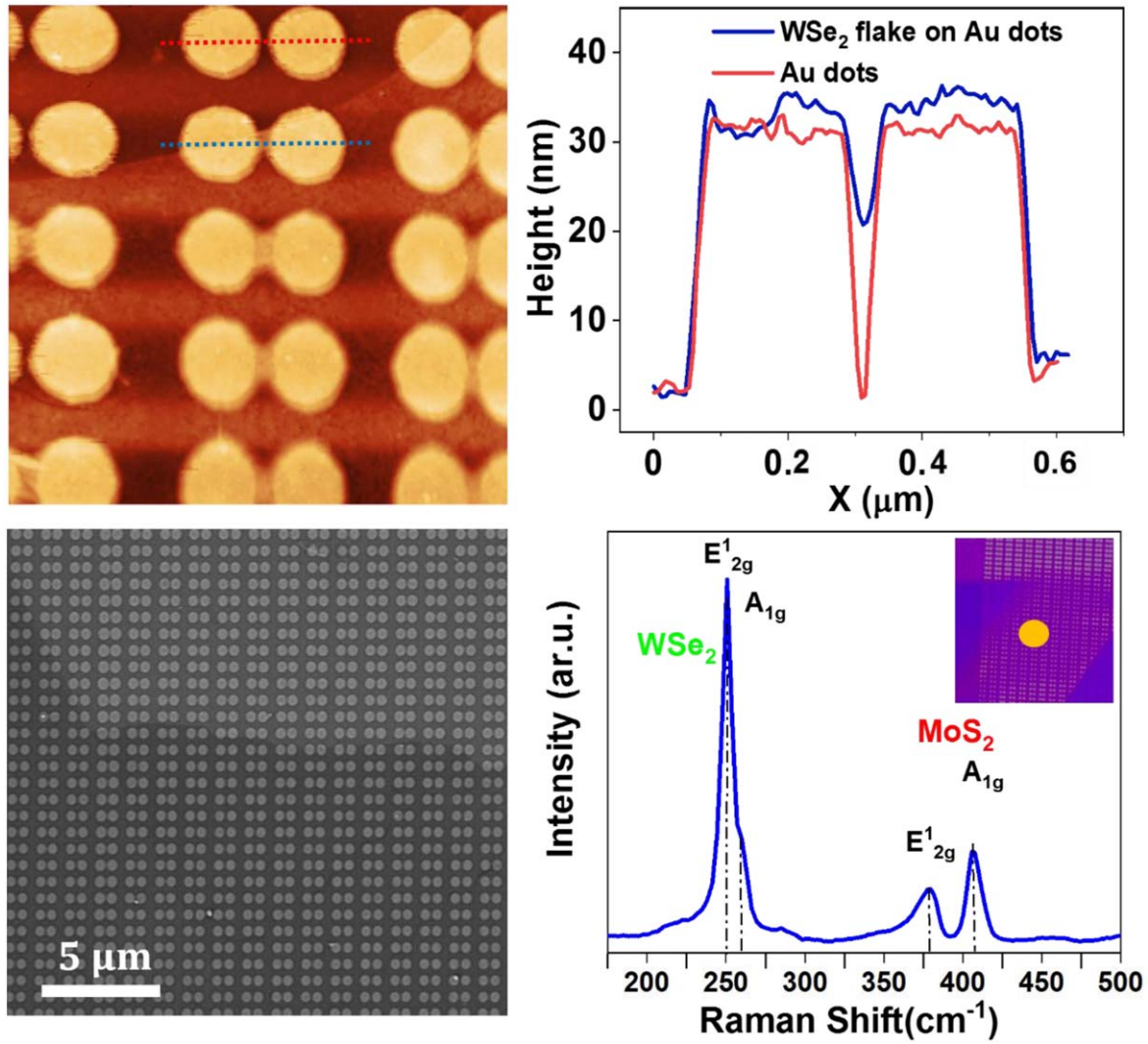
Figure 2. (a) AFM image of WSe$_2$/Au nanoarrays. (b) The AFM step-height profiles for Au dots (red line) and WSe$_2$/Au nanodots (blue line). (c) SEM image of WSe$_2$/Au nanoarrays. (the black area shows WSe$_2$/Au nanoarrays and the gray region is corresponding to Au nanoarrays.) (d) Raman spectrum of WSe$_2$/MoS$_2$ /Au nanoarrays (The pronounced peak at ~250 cm^{-1} assigns to WSe$_2$ and peaks at ~380 and ~410 cm^{-1} are attributing to MoS$_2$ flake).

intermediate applied voltage, the direct tunneling current is proportional to the voltage, expressed by [29, 30]:

$$I \propto V \exp\left(-\frac{2d\sqrt{2m^*\phi}}{\hbar}\right), \tag{1}$$

Where d, m^*, $\hbar$ and ϕ are the tunneling thickness, effective electron mass, reduced Planck constant and tunneling barrier, respectively. Although in this case, there is no Fowler-Nordheim (FN) tunneling, we can still use the threshold voltage of the FN tunneling to calculate the energy barrier. The threshold voltage, $V_{th} \simeq 0.2$ V, corresponds to ϕ/e. Therefore, the ϕ can be estimated as ~0.2 eV. Using the direct tunneling formula, where $m^* \sim 0.5$ m$_0$ [31], we get $d_1 \simeq 0.4$ nm and $d_2 \simeq 0.2$ nm in the first and second regimes (See inset of figure 3(b)). Due to the monolayer nature of WSe$_2$ and MoS$_2$ flakes, the thickness of these layers is about ~ 1 nm. Hence, the formation of 0.4 nm and 0.2 nm of depletion layers is reasonable [30]. As the V_{ds} increases, the depletion layer thickness decreases, which facilities more electrons and holes tunneling. Photoresponse dependency to light power intensity under illumination of 445 nm is displayed in Fig. S6.

To investigate the effect of electrostatic doping, the I_{sd} was monitored by swiping gate voltages at a constant applied $V_{sd} = +4$ V (figure 4(a) and fig. S7). For a positive gate voltage, the electrical field created in heterojunction, assists the charges separation which causes more charge carriers.

However, the negative gate voltages, prevents separation of charge carriers and so the electrical conduction decreases. The field-effect mobility of charge carriers was calculated as ~10 cm^{2}V^{-1} s^{-1} through the following equation [32]

$$\mu = [dI_{ds}/dV_g] \times [L/(WC_iV_{ds})], \tag{2}$$

where L and W are the length and width of the device channel, respectively. The C_i is the capacitance of the gate oxide ($C_i = 1.17 \times 10^{-4}$ Fm^{-2} for 300 nm SiO$_2$), and the V_g represents the applied back gate voltage. It worthy to mention that the Au nanoarrays are screening some part of the
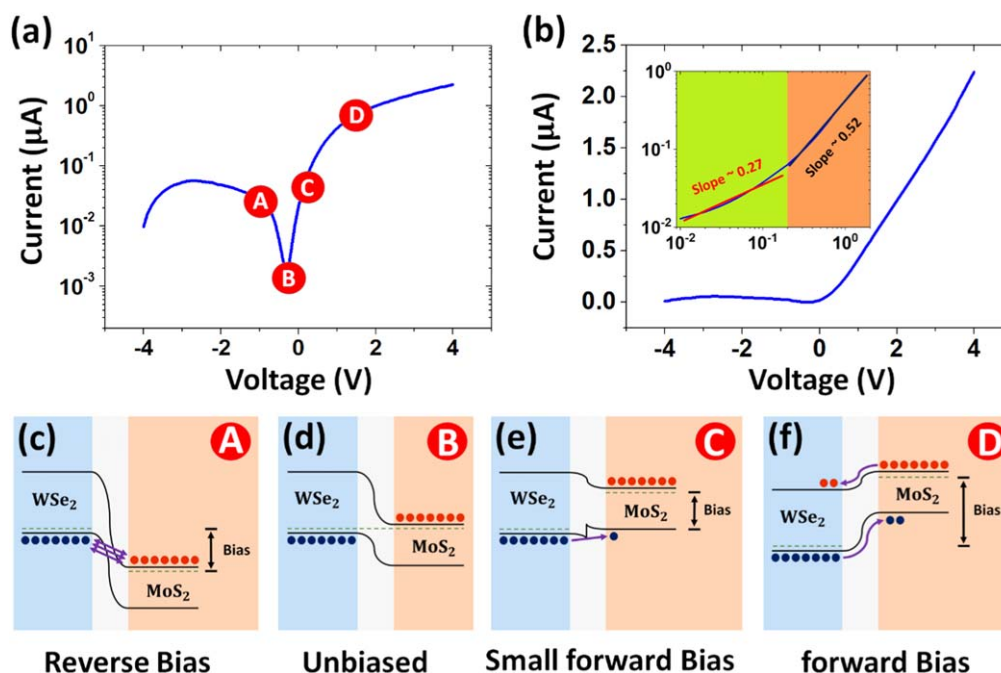
Figure 3. $I-V$ characteristics of the device, on linear (a) and logarithmic (b) scales. (c) Energy band diagram at a reverse bias, which causes BTBT phenomenon. (d) Energy band diagram at unbiased mode which no current will be measured. (e) Energy band diagram at small forward bias, which holes transferred and participate in conduction. (f) Energy band diagram at a forward bias, in which electrons and holes are transferred and participate in conduction. (g) $I-V$ characteristic of the $MoS_2/WSe_2/Au$ nanoarrays in double-log scale.

heterostrucutre and make in-plane homojunction which may modify concentration/type of the charge carriers. This should be taken into account in electrical characterizations of denser Au nanoarrays and nanometer scale electrodes.

To study the photoresponse of the device, the $I-V$ characteristic by no electrical gate (figure 4(b)) and applying gate voltage of $+ 10$ V, were measured under the illumination of different wavelengths (figure 4(c) and Fig. S7). As observed, the gate voltage noticeably enhances the photocurrent due to more separation of the charge carriers. Besides, as we move toward shorter wavelengths (<500 nm), the photons with more energies excite more free and hot electrons in the Au nanoarrays due to the localized surface plasmons resonance (LSPR) effect. These hot electrons can easily break the potential barriers and inject to the conduction band of the heterostructure [33].

The Au nanoarrays play two important roles during light irradiation. Each of the Au nanoparticles individually can absorb light due to the LSPR effect. It is well known that light absorption by LSPR depends on the dielectric properties of the medium and geometry of the particles such as diameter and height. For particles larger than 100 nm in diameter, light absorption occurs over a wide range of visible and ultraviolet regions [34]. In the case of a particle diameter of 250 nm, the maximum absorption wavelength is in the range of 395 to 580 nm (Fig. S8) [33]. This absorption of light is coming from collective oscillations of free electrons in Au nanoparticle which causes to decay of the surface plasmons and hot electrons generation. The Plasmonic nanostructures exhibit tunable Fano resonances, which leads to strongly suppressing of light scattering and hot electron generation.

The hot electrons may transfer from plasmonic islands into the WSe_2 /MoS_2 heterostructure and consequently have contribution in photocurrent. In addition, the strengthened near field associated with plasmons are capable of efficiently enhancing the excitation of electrons and holes in heterostructures accompanied by reducing their recombination.

In contrast to isolated or single plasmonic particles, the dimer structure shows a much larger absorption cross-section resulting in larger electrical field enhancements. In other words, the binary-fold hot spots lead to increased yield of hot electrons injection and more separation of the electron−hole pairs by light irradiation. The dimer form of Au nanoarrays has an asymmetric structure on the substrate. In the strong coupling state of the LSPR with incident light, polarization dependence of the photocurrent generation can be expected. To study this effect, two linear polarizations of light (parallel to dimer axis of Au array indexed as ∥ and perpendicular to it marked as ⊥, (figure 5(a))) was irradiated on the sample as a normal angle in similar intensity conditions. As it can be seen in figure 5(b), the effect of polarization of incidence light was significant on photocurrent in the wavelength range of 395 to 580 nm. This highlights the plasmonic effect of Au nanoarrays on photocurrent enhancement due to carrier multiplication.

In parallel polarization of the incidence light, the small spatial gap between the Au nanoparticles interacts with the electromagnetic oscillations. In addition to hot electrons generation and then injection into the heterostructure, it creates an intensified local electrical field at the inter-distances of the dimer gaps because of overlapping of the surface plasmons decay. The intensified local electric field supports more
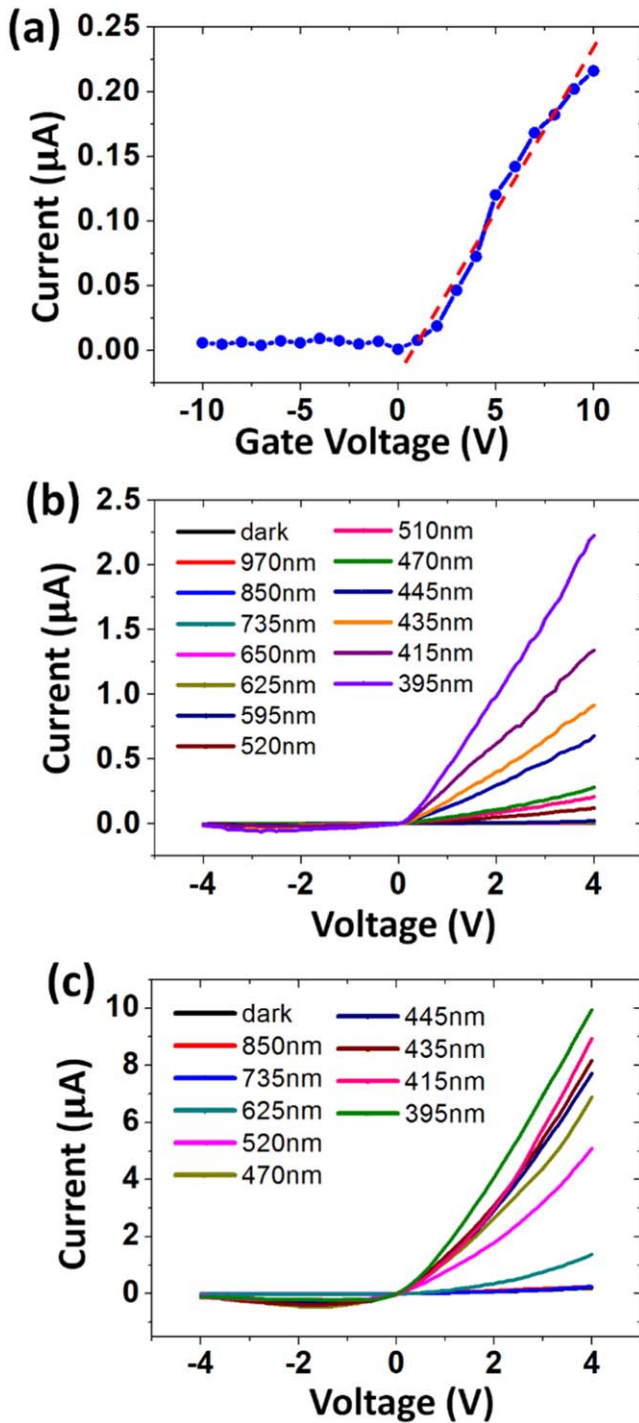
Figure 4. (a) The effect of gate voltage on the current of the device. (b) Photocurrent *I*−*V* curves without applying gate voltage. (c) Photocurrent *I*−*V* curves of the device at +10 V applied gate.

Figure 5. (a) Specification of ⊥ and ∥ polarization on the SEM image of the device. (b) The effect of ⊥ and ∥ polarizations on the generation of charge carriers. (c) Schematic illustration of photo-generated charge carriers in dimer Au nanoparticles and transferring to the WSe₂ and MoS₂ layers.

separation of photoinduced carriers on flakes heterojunction [35, 36].

In consistent with theoretical predictions and experimental suggestions on dimer plasmonic structures, the larger gap between the Au dimers causes a blue shift of optical absorption and the lower gap/diameter ratio causes more absorption than single plasmonic nanoparticles [37–39]. In the current device, the physical gap/particle diameter ratio is
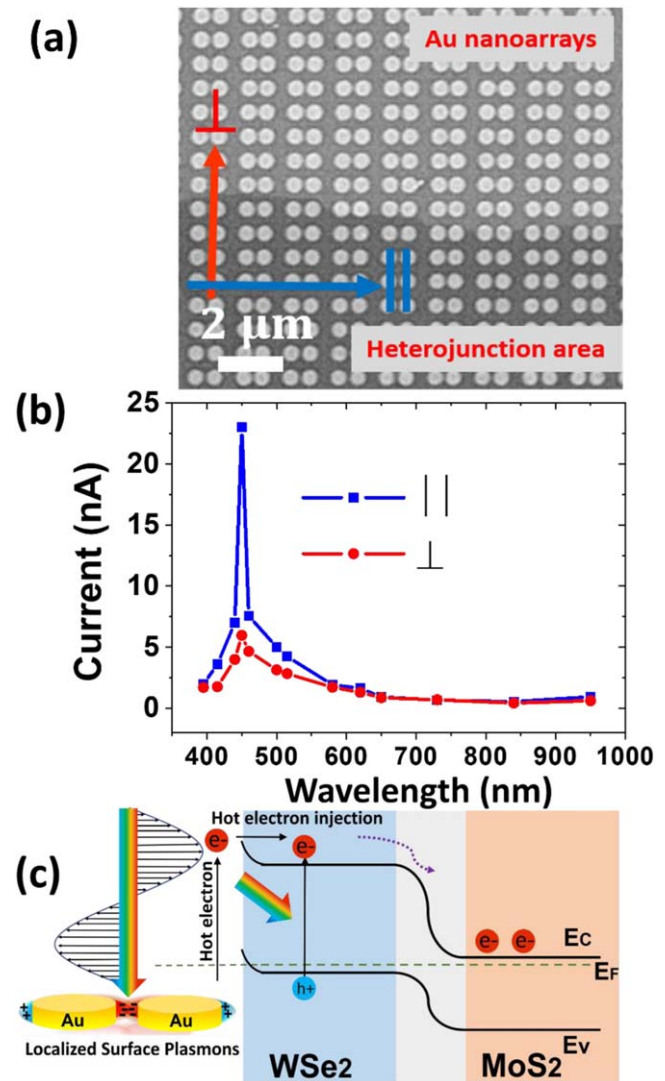
0.1 which leads to four times photocurrent amplification than another polarization [39]. The effect of hot spots in dimer Au nanoparticles on photogenerated charge carriers is schematically depicted in figure 5(c).

Due to these facts, in the parallel direction, polarized incident photons can be well coupled with the LSPR of the Au dimers which remarkably yielding high electrical field enhancement factors [40]. As mentioned above, this intensified near field can efficiently separate the photogenerated electron and holes in the flakes and postpone recombination of the charge carriers. However, in another ⊥ direction, these photocurrent multiplications are diminished because of the weaker coupling and overlapping of the surface plasmons (figure 5(b)). Therefore, the LSPR can have significant contribution in photoresponse of the photodetector in the wavelength range of 395 to 580 nm.
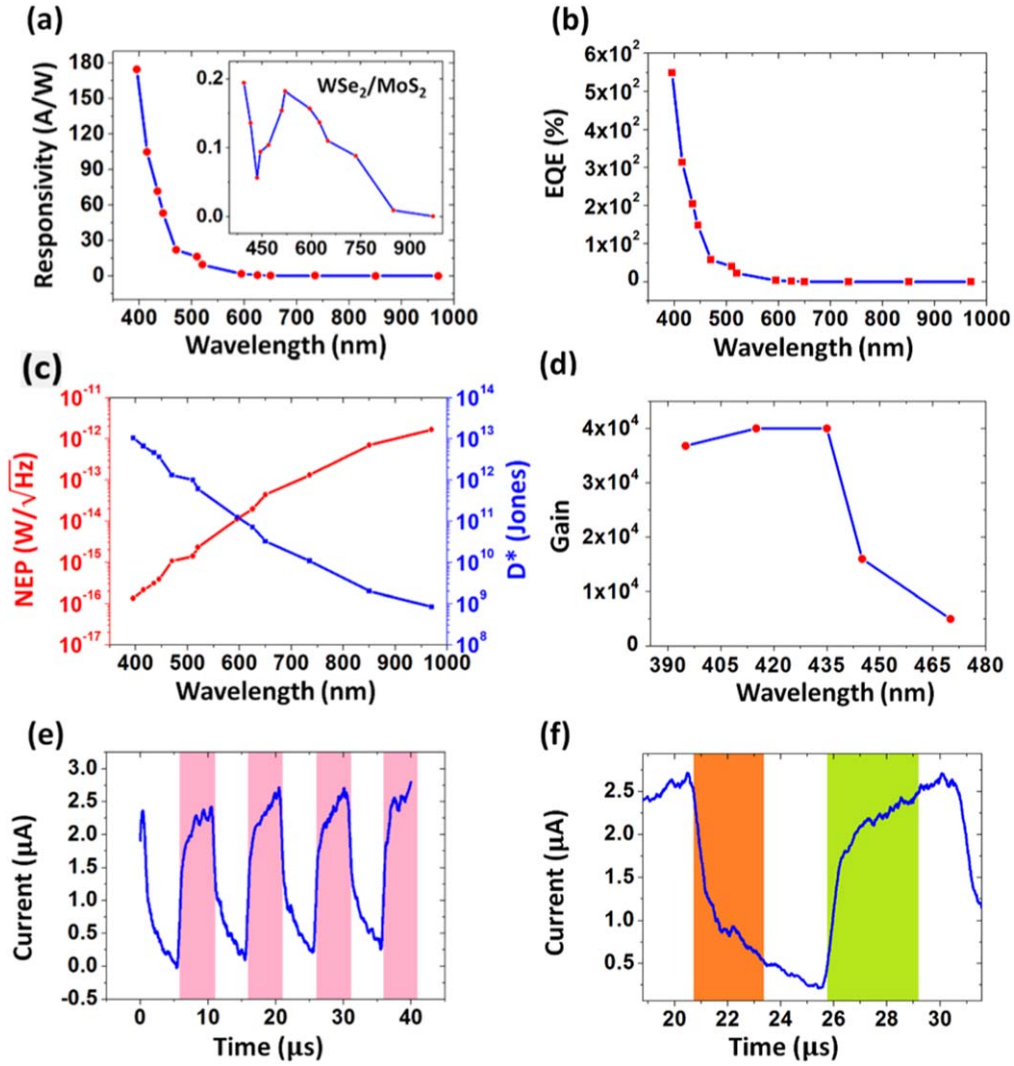
Figure 6. (a) Responsivity as a function of LED irradiance at different wavelengths at $V_g = 0V$ and $V_{ds} = +4V$, (inset depicts the responsivity of WSe$_2$/MoS$_2$ device with no Au nanoarrays). (b) External Quantum efficiency (EQE) as a function of LED irradiance at different wavelengths at $V_g = 0$ V and $V_{ds} = +4$ V. (c) Spectral dependence of the NEP and specific detectivity (D^*) of the device. (d) Gain as a function of LED irradiance at different wavelengths of $V_g = 0$ V and $V_{ds} = +4$ V. (e) The response of the device to a pulsed light (395 nm) source (the turn on and turn off times are 5 μs.) (f) Rising and falling times of the device at pulsed light (395 nm) source (the turn on and turn off times set as 5 μs.).

In figure 6, under the illumination of unpolarized LEDs light at different wavelengths, the photodetection results of the heterostructure device are presented including photoresponsivity (R), EQE, noise equivalent power (NEP), specific detectivity (D^*) and photoconductivity gain (G). The Photoresponsivity (R) defined as the ratio of produced photocurrent to the incident light power as.

$$R = (J_{ph}—J_d)/P_{in} \tag{3}$$

Where J_{ph} and J_d are the current density under light irradiation and dark states, respectively. The P_{in} denotes the optical power density of the incident light.

The photoresponsivity of the device is shown in figure 6(a) for the wavelengths range from 395 to 970 nm. As it can be seen, in shorter wavelength of 550 nm, the photoresponsivity of the device reaches to a value of 9.4 A W^{-1} at 520 nm to 174 A/W for 395 nm, which represents a 188-fold

and 3480-fold improvement, respectively [22]. Although the device responds to incident photons in wide ranges of the wavelengths (from 395 to 970 nm), its maximum photoresponsivity is in the range of 395 to 520 nm. As mentioned above, apart from well energy band alignment of the WSe$_2$/MoS$_2$ heterostructure, the main feature behind this considerable photoresponsivity attributes to the hot electrons and intensified local filed coming from the presence of the dimer Au nanoarrays underneath of the heterostructure.

The EQE parameter is the ratio of the number of the collected charge carriers (N$_C$) to the number of photons (N$_I$) irradiated on the device as following:

$$EQE = (N_C/N_I) = (hcR/e\lambda), \tag{4}$$

where h is Planck constant, c represents the speed of light, e is the electron charge, and λ is the wavelength of the incident light.

Table 1. Performance of current devices in comparison with similar structures.

Structures	Wavelength [nm]	Responsivity [A/W]	Response time	References
MoS_2	Visible	7.5×10^{-3}	50 ms	[42]
MoS_2	UV-Visible	6.3×10^{-5}	20 ms	[43]
WSe_2	Visible	4.4×10^{-2}	5.5×10^{-9} s	[44]
WSe_2/MoS_2	514–633	0.05	—	[22]
G - GQDs	532–10,000	861–0.4	30 s	[45]
$WSe_2/$ GaSe	520	6.2	30 μs	[46]
G/ Si Nanorods/ Au NPs	850	1.5	73 μs	[47]
ZnO NWs/ Al NPs	367	1.59	40 s	[48]
ZnSe NWs/ Ag NPs	480	1.85×10^{-1}	—	[49]
WSe_2/MoS_2	Visible	0.2	—	This work
WSe_2/MoS_2 / Au nanoarrays	395–520	15–180	2.5 μs	This work

The figure 6(b) illustrates the EQE as a function of wavelengths of the incidence light. Due to the direct relationship between the R and EQE parameters, amazing improvement as high as 549% at 395 nm obtained which is a remarkable in comparison to similar heterostructure of WSe_2/MoS_2 reported before [22].

The evaluated NEP parameter defines as the minimum light signal power which can be detected from the total noise by a photodetector is shown in figure 6(c). In other words, the NEP represents required optical input power to achieve a signal-to-noise ratio (SNR) of one within a bandwidth of 1Hz. The NEP is calculated as:

$$\text{NEP} = \frac{\sqrt{S_I}}{R}, \ (S_I = S_I(1/f) + S_I(\text{shot}) + S_I(\text{thermal})),$$

$$(5)$$

Where R shows Responsivity and S_I is the total spectral density. As it can be seen in figure 6(c), the NEP values vary from 10^{-12} to 10^{-16} in the wavelength range of 970 to 395 nm. (See S6) The sensitivity of photodetector depending on different parameters such as bandwidth, device geometry and effective surface area of the detector which can be expressed in specific detectivity (D^*). This parameter estimated by:

$$D^* = \sqrt{A} / \text{NEP} \qquad (6)$$

where A is the area of the photodetector. The data in figure 6(c) indicates that the D^* rises from 10^9 to 10^{13} in the wavelength range of 970 nm to 395 nm which is important results.

The G parameter presents the ratio of the detected charge carriers per single incident photons and is given by:

$$G = \tau_{\text{life}} / \tau_{\text{transit.}} \qquad (7)$$

In this ratio, τ_{life} defined as $\tau_{\text{life}} = L^2/\mu V_{\text{ds}}$, where L is the length of the channel and μ is the carrier mobility. The τ_{transit} is approximated by the falling time of the transient J_{ph} during ON/OFF cycles of illumination [35]. Regard to the G values reported in figure 6(d), in the range of 395 nm to 470 nm more photocurrent is produced in the photodetector leading to larger photoconductive gains. Therefore, at smaller wavelengths of 435 nm, high photoconductive gain (~4×10^4) can be seen while for wavelengths longer than 435 nm, it drops to 1×10^4.

In figure 6(e), the response of the device to the pulsed irradiated light has been reported. The wavelength of light was 395 nm (for other wavelengths see Fig. S10), and the turn-on (marked as pink regions) time was 5 μs equal to the turn off time (white regions). From the response time of the device in one cycle of light exposure (figure 6(f)), one can estimate rising and falling times. The rising time (time interval from increasing of the signal from 10% to 90% of the peak value) which is exhibited as the green color region in figure 6(f) and falling time (decreasing of the signal from 90% to 10% of the peak value) displaying as orange color region, were measured as fast as 2.5 μs and 3.5 μs, respectively. This reflects rapid photoinduced carrier generation and transport through the device.

In table 1, the photodetector parameters of this study named as WSe_2/MoS_2 /Au nanoarrays have been compared with similar reported devices. The reference WSe_2/MoS_2 device with no Au nanoarrays was also fabricated and optoelectronic properties have been studied (Fig. S9). As it can be observed, the major challenges of heterostructures are their small photoresponsivity, EQE and response/falling times. However, the presence of the Au dimer nanoarrays has a great promotion on the photoresponsivity of the device within a few microsecond times scales. This photoresponse enhancement is mainly assigned to three mechanisms: (1) Heterojunction of energetically well-matched TMDs on plasmonic arrays drastically enriches the light interactions. More interaction of light with TMDs leads to more optical energy absorption rather than dissipating in the surrounding space which results in more photoinduced electron and hole [41]. (2) by light irradiation in wavelengths ranges of LSPR coupling with noble particle geometry, the free electrons as plasmonic waves oscillate at a resonance frequency. This creates a local electric field as hot spots on the surface of the nanoparticles, which increases the separation of the photo-induced charge carriers in the heterostructure. (3) The hot electrons generated from plasmonic coupling in the nanoparticles, cross through the potential barrier of the nanoparticles and can have involvement in increasing of electrical conduction [35, 36, 41].

It is worthy to note that when noble metallic nanoparticles such as Au, Ag, and Al are used in photodetectors,

as an important obstacle for the fabrication of fast switchable photodetectors the response time of these systems increases due to carrier scattering at the interfaces [45, 48]. Here, simultaneous using ordered Au nanoarrays and WSe$_2$/MoS$_2$ heterostructure, less carrier recombination and rapid charge transferring to the electrodes can be occurred [50]. This reduces the system response time as fast as 2.5 μs, which is a considerable record for photodetectors containing plasmonic nanoparticles. Regard to table 1, the presented device in this research showed exceptional values to most of the photo-detection parameters. Therefore, it can be supposed that the introduced approach as WSe$_2$/MoS$_2$ /Au nanoarrays device is applicable for the fabrication of rapid and high perfomance photodetectors.

4. Conclusion

In summary, the improvement of photoresponsivity of atomically thin WSe$_2$/MoS$_2$ heterostructure on Au nanoar-rays has been investigated using plasmon-induced photo-carriers. Due to the LSPR effect in dimer arrays of the Au nanoparticles act as an active and light-harvester substrate for WSe$_2$/MoS$_2$ heterojunction. This approach indicated a high photoresponsivity (174 A W^{-1}), high external quantum efficiency (549%), and fast response time (2.5–3.5 μs) for fabricated photodetectors. The operation mechanism behind this photodetectivity enhancement can be assigned to increasing light interactions at heterostructure, hot electron generations and efficient charge separations because of the intensified local field. The introduced structure is a model for merging the novel characteristics of plasmonic nanoparticles and tunable photonic properties of TMDs heterostrucutres which can open up a new pathway to ultra-fast and sensitive optoelectronic devices.

Acknowledgments

Data availability statement

All data that support the findings of this study are included within the article (and any supplementary files).

Author disclosure statement

The authors declare no competing financial and conflicts of interest.

ORCID iDs

Ali Esfandiar ● https://orcid.org/0000-0002-7566-9791

References

[1] Novoselov K 2004 Electric field effect in atomically thin carbon films *Science* **306** 666–9

[2] Bernardi M, Ataca C, Palummo M and Grossman J 2017 Optical and electronic properties of two-dimensional layered materials *Nanophotonics* **6** 479–93

[3] Winkler C, Harivyasi S and Zojer E 2018 Controlling the electronic properties of van der waals heterostructures by applying electrostatic design *2D Materials* **5** 035019

[4] Iqbal M, Elahi E, Amin A, Hussain G and Aftab S 2020 Chemical doping of transition metal dichalcogenides (TMDCs) based field effect transistors: a review *Superlattices Microstruct.* **137** 106350

[5] Long M, Wang P, Fang H and Hu W 2018 Progress, challenges, and opportunities for 2D material based photodetectors *Adv. Funct. Mater.* **29** 1803807

[6] He J, Tao L, Zhang H, Zhou B and Li J 2019 Emerging 2D materials beyond graphene for ultrashort pulse generation in fiber lasers *Nanoscale* **11** 2577–93

[7] Das S, Pandey D, Thomas J and Roy T 2018 The role of graphene and other 2D materials in solar photovoltaics *Adv. Mater.* **31** 1802722

[8] Wang Z, Jingjing Q, Wang X, Zhang Z, Chen Y, Huang X and Huang W 2018 Two-dimensional light-emitting materials: preparation, properties and applications *Chem. Soc. Rev.* **47** 6128–74

[9] Wang J, Verzhbitskiy I and Eda G 2018 Electroluminescent devices based on 2D semiconducting transition metal dichalcogenides *Adv. Mater.* **30** 1802687

[10] Shen W, Hu C, Huo S, Sun Z, Fan S, Liu J and Hu X 2018 Wavelength tunable polarizer based on layered black phosphorus on Si/SiO$_2$ substrate *Opt. Lett.* **43** 1255

[11] Sun Y, Wang D and Shuai Z 2016 Indirect-to-direct band gap crossover in few-layer transition metal dichalcogenides: a theoretical prediction *J. Phys. Chem.* C **120** 21866–70

[12] Wurstbauer U, Miller B, Parzinger E and Holleitner A 2017 Light–matter interaction in transition metal dichalcogenides and their heterostructures *J. Phys. D: Appl. Phys.* **50** 173001

[13] Cui X *et al* 2015 Multi-terminal transport measurements of MoS$_2$ using a van der Waals heterostructure device platform *Nat. Nanotechnol.* **10** 534–40

[14] Wang Q, Lai J and Sun D 2016 Review of photo response in semiconductor transition metal dichalcogenides based photosensitive devices *Opt. Mater. Express* **6** 2313

[15] Lee C *et al* 2014 Atomically thin p–n junctions with van der Waals heterointerfaces *Nat. Nanotechnol.* **9** 676–81

[16] Ceballos F, Bellus M, Chiu H and Zhao H 2014 Ultrafast charge separation and indirect exciton formation in a MoS2–MoSe2 van der Waals Heterostructure *ACS Nano* **8** 12717–24

[17] Li C, Cao Q, Wang F, Xiao Y, Li Y, Delaunay J and Zhu H 2018 Engineering graphene and TMDs based van der Waals heterostructures for photovoltaic and photoelectrochemical solar energy conversion *Chem. Soc. Rev.* **47** 4981–5037

[18] Rao G *et al* 2019 Two-dimensional heterostructure promoted infrared photodetection devices *InfoMat* **1** 272–88

[19] Wei X, Yan F, Shen C, Lv Q and Wang K 2017 Photodetectors based on junctions of two-dimensional transition metal dichalcogenides *Chin. Phys.* B **26** 038504

[20] Xu K *et al* 2018 The role of Anderson's rule in determining electronic, optical and transport properties of transition metal dichalcogenide heterostructures *Phys. Chem. Chem. Phys.* **20** 30351–64

[21] Flöry N, Jain A, Bharadwaj P, Parzefall M, Taniguchi T, Watanabe K and Novotny L 2015 A WSe2/MoSe2 heterostructure photovoltaic device *Appl. Phys. Lett.* **107** 123106

[22] Cheng R, Li D, Zhou H, Wang C, Yin A, Jiang S, Liu Y, Chen Y, Huang Y and Duan X 2014 electroluminescence and photocurrent generation from atomically sharp WSe2/MoS2 heterojunction p–n diodes *Nano Lett.* **14** 5590–7

[23] Pak S *et al* 2017 Strain-mediated interlayer coupling effects on the excitonic behaviors in an epitaxially grown MoS2/WS2 van der Waals Heterobilayer *Nano Lett.* **17** 5634–40

[24] Desai S, Seol G, Kang J, Fang H, Battaglia C, Kapadia R, Ager J, Guo J and Javey A 2014 Strain-Induced Indirect to Direct Bandgap Transition in Multilayer WSe2 *Nano Lett.* **14** 4592–7

[25] Furchi M, Pospischil A, Libisch F, Burgdörfer J and Mueller T 2014 Photovoltaic Effect in an Electrically Tunable van der Waals Heterojunction *Nano Lett.* **14** 4785–91

[26] Chiu M, Zhang C, Shiu H, Chuu C, Chen C, Chang C, Chen C, Chou M, Shih C and Li L 2015 Determination of band alignment in the single-layer MoS2/WSe2 heterojunction *Nature Commun.* **6** 7666

[27] Hosseini S, Esfandiar A, Iraji Zad A, Hosseini-Shokouh S and Mahdavi S 2019 High-ponsive backward diode by two-dimensional SnS2/silicon heterostructure *ACS Photon.* **6** 728–34

[28] Lee H, Ahn J, Shim W, Im S and Hwang D 2018 2D WSe2/MoS2 van der Waals heterojunction photodiode for visible-near infrared broadband detection *Appl. Phys. Lett.* **113** 163102

[29] Ikuno T, Okamoto H, Sugiyama Y, Nakano H, Yamada F and Kamiya I 2011 Electron transport properties of Si nanosheets: transition from direct tunneling to fowler-nordheim tunneling *Appl. Phys. Lett.* **99** 023107

[30] Doan M, Jin Y, Adhikari S, Lee S, Zhao J, Lim S and Lee Y 2017 Charge transport in MoS2/WSe2van der Waals Heterostructure with tunable inversion layer *ACS Nano* **11** 3832–40

[31] Rasmussen F and Thygesen K 2015 Computational 2D materials database: electronic structure of transition-metal dichalcogenides and oxides *J. Phys. Chem.* C **119** 13169–83

[32] Huang J, Yang L, Liu D, Chen J, Fu Q, Xiong Y, Lin F and Xiang B 2015 Large-area synthesis of monolayer WSe2 on a SiO2/Si substrate and its device applications *Nanoscale* **7** 4193–8

[33] Shafiqa A, Abdul Aziz A and Mehrdel B 2018 Nanoparticle optical properties: size dependence of a single gold spherical nanoparticle *J. Phys.: Conf. Series* **1083** 012040

[34] Kim H and Lee D 2018 Near-infrared-responsive cancer photothermal and photodynamic therapy using gold *Nanoparticles Polym.* **10** 961

[35] Ni Z *et al* 2017 Plasmonic silicon quantum dots enabled high-sensitivity ultrabroadband photodetection of graphene-based hybrid phototransistors *ACS Nano* **11** 9854–62

[36] Huang J and Luo L 2018 low-dimensional plasmonic photodetectors: recent progress and future opportunities *Adv. Opt. Mater.* **6** 1701282

[37] Marhaba S, Bachelier G, Bonnet C, Broyer M, Cottancin E, Grillet N, Lermé J, Vialle J and Pellarin M 2009 Surface plasmon resonance of single gold nanodimers near the conductive contact limit *J. Phys. Chem.* C **113** 4349–56

[38] Atay T, Song J and Nurmikko A 2004 Strongly interacting plasmon nanoparticle pairs: from dipole−dipole interaction to conductively coupled regime *Nano Lett.* **4** 1627–31

[39] Zhang W, Li Q and Qiu M 2013 A plasmon ruler based on nanoscale photothermal effect *Opt. Express* **21** 172

[40] Kravets V, Kabashin A, Barnes W and Grigorenko A 2018 Plasmonic surface lattice resonances: a review of properties and applications *Chem. Rev.* **118** 5912–51

[41] Wang J, Fang H, Wang X, Chen X, Lu W and Hu W 2017 Recent progress on localized field enhanced two-dimensional material photodetectors from ultraviolet-visible to infrared *Small* **13** 1700894

[42] Yin Z, Li H, Li H, Jiang L, Shi Y, Sun Y, Lu G, Zhang Q, Chen X and Zhang H 2011 Single-layer MoS2 phototransistors *ACS Nano* **6** 74–80

[43] Lee Y, Yang J, Lee D, Kim Y, Park J, Kim H and Cho J 2016 Trap-induced photoresponse of solution-synthesized MoS2 *Nanoscale* **8** 9193–200

[44] Massicotte M, Schmidt P, Vialla F, Schädler K, Reserbat-Plantey A, Watanabe K, Taniguchi T, Tielrooij K and Koppens F 2015 Picosecond photoresponse in van der Waals heterostructures *Nat. Nanotechnol.* **11** 42–6

[45] Zhang B, Liu T, Meng B, Li X, Liang G, Hu X and Wang Q 2013 Broadband high photoresponse from pure monolayer graphene photodetector Nature *Communications* **4**

[46] Wei X, Yan F, Lv Q, Shen C and Wang K 2017 Fast gate-tunable photodetection in the graphene sandwiched WSe2/GaSe heterojunctions *Nanoscale* **9** 8388–92

[47] Luo L, Zeng L, Xie C, Yu Y, Liang F, Wu C, Wang L and Hu J 2014 Light trapping and surface plasmon enhanced high-performance NIR photodetector *Sci. Rep.* **4** 3914–8

[48] Lu J, Xu C, Dai J, Li J, Wang Y, Lin Y and Li P 2015 Improved UV photoresponse of ZnO nanorod arrays by resonant coupling with surface plasmons of Al nanoparticles *Nanoscale* **7** 3396–403

[49] Wang L, Chen R, Ren Z, Ge C, Liu Z, He S, Yu Y, Wu C and Luo L 2016 Plasmonic silver nanosphere enhanced ZnSe nanoribbon/Si heterojunction optoelectronic devices *Nanotechnology* **27** 215202

[50] Nguyen P *et al* 2019 Visualizing electrostatic gating effects in two-dimensional heterostructures *Nature* **572** 220–3